Journal of
Materials Chemistry C

ROYAL SOCIETY
OF CHEMISTRY

PAPER

View Article Online
View Journal

Check for updates

Cite this: DOI: 10.1039/d5tc03145a

Efficiently doped P3HT and polystyrene blend with porous 3D structure for thermoelectric applications

Souhail Essadiki,[a] Alain Carvalho,[a] Fabrice Vigneron,[b] Guillaume Fleith,[a] Jérôme Combet,[a] Doru Constantin,[a] Nicolas Stein[c] and Laure Biniek*[a]

Received 20th August 2025,
Accepted 29th October 2025

DOI: 10.1039/d5tc03145a

rsc.li/materials-c

This study describes a reproducible process for forming highly mesoporous, mechanically robust, and handleable aerogels based on entangled poly(3-hexylthiophene) (P3HT) and syndiotactic polystyrene (sPS) nanofibers for thermoelectric applications. The highly porous structure results in low thermal conductivity, allowing the temperature difference (between the hot and the cold side) to be maintained across the aerogel sample. Porosity also enables dopants to diffuse efficiently within the sample. When using 2,3,5,6-tetrafluoro-7,7,8,8-tetracyano-quinodimethane (F_4TCNQ), the highest dopant uptake leads to a maximum apparent electrical conductivity of 2×10^{-2} S cm^{-1} and a Seebeck coefficient (58 μV K^{-1}) close to the values obtained in thin films. The Seebeck coefficient is not affected by the high porosity of the material. To improve the doping level of the P3HT:sPS aerogels, $FeCl_3$ or a mixture of F_4TCNQ:$FeCl_3$ is also used as a dopant. This enhances the power factor (0.2 μW m^{-1} K^{-2}) without significantly increasing the thermal conductivity (30–40 mW m^{-1} K^{-1}). Finally, the use of the doped aerogel as a vertical thermoelectric generator with one leg is demonstrated by generating a few tens of nW at a thermal difference of 11 K. This result highlights the potential for integrating these polymer aerogels into wearable thermoelectric generators for powering microelectronics.

Introduction

Organic thermoelectric (TE) materials, mostly based on π-conjugated polymers, offer a promising route for harvesting low-grade waste heat, especially in room-temperature applications. This is becoming attractive with the rise of wearable and flexible electronics.[1,2] Their tunable molecular structures, low thermal conductivity, cost-efficiency, and mechanical flexibility make them ideal candidates for energy harvesting in flexible electronics.[3,4] Achieving a high thermoelectric figure of merit (ZT) remains essential. Optimizing the ZT of materials includes maximizing their Seebeck coefficient (S) and electrical conductivity (σ), while minimizing their thermal conductivity (κ), as $ZT = \frac{\sigma S^2}{\kappa}T$. These parameters are often interdependent, making simultaneous optimization challenging. As a result, most research has centred on improving the power factor (PF = σS^2), whereas thermal conductivity reduction has received comparatively less attention. Strategies for enhancing PF focus on improving charge transport properties of the polymer and doping efficiency,[5] and include macromolecular engineering,[6–8] chemical doping conditions[9,10] or structural tailoring of π-conjugated polymers.[11,12]

Another approach to enhancing the TE performance of π-conjugated polymers is by introducing ordered porosity in their structure. In such nanostructures, phonon scattering can help reduce κ without significantly reducing σ. As a recent example, imprinted porous films (with 25% porosity) of PDPPSe-12 (a π-conjugated polymer based on diketopyrrolopyrrole) exhibit half the thermal conductivity of pristine films, while maintaining nearly unaffected power factors.[13] In parallel, the interest in aerogels (3-dimensional porous materials with a high porosity and surface area) in TE is growing.[14–16] Their unique structure can lead to an ultra-low κ, and provide a lever for optimizing the ZT, as well as for maintaining a temperature gradient throughout the sample. As additional advantages, their structure can be integrated into vertical TE module architectures or modular shapes (surfaces/thickness), and sometimes with flexible properties. Different production techniques for bulk and porous materials are reported in the literature, resulting in a wide variety of structures, including cryogels, foams, and aerogels with more or less controlled pore sizes and shapes.

Gordon *et al.* reported, for the first time, the fabrication of porous PEDOT:PSS by rehydrating thick films followed by

---

[a] *Université de Strasbourg, CNRS, Institut Charles Sadron UPR22, F-67000 Strasbourg, France. E-mail: laure.biniek@ics-cnrs.unistra.fr*

[b] *Institut de Chimie et Procédés pour l'Énergie, l'Environnement et la Santé, CNRS-Université de Strasbourg, UMR7515, Strasbourg, France*

[c] *Université de Lorraine, CNRS, IJL, F-57000 Metz, France*

freeze-drying. Even though the method yielded a gradient of pore sizes and shapes throughout the sample thickness, the electrical conductivity for the non-treated film was maintained at 35 S cm^{-1} because of a moderate density of 0.25 g cm^{-3}. The thermal conductivity was not measured in such films.[17] Weinbach *et al.* successfully obtained a macroporous unidirectional honeycomb-like structure using the ice-templating technique, resulting in a low value of κ = 37 mW m^{-1} K^{-1} but a limited σ of 1.2 S cm^{-1} (due to the low density of 0.03 g cm^{-3}).[18] Feng *et al.* combined the ice-templating method with a thawing process in an H_2SO_4 solution, which enhances the electrical conductivity of the macroporous sample to 12 S cm^{-1} along the freezing direction.[19] Baysal *et al.* used omnidirectional 3D printing followed by freeze-drying to produce stretchable PEDOT:PSS aerogels with a κ value of 65 mW m^{-1} K^{-1}. The 3D printed pillars generated a high thermoelectric power density of 26 nW cm^{-2} under conditions mimicking a wearable device attached to the skin and operating indoors.[20] Controlling the self-assembly of the polymer chains and the freezing conditions is necessary in order to tune the final porous structures and thus to optimize their properties. The porosity achieved by the freeze-drying technique is in the range of macropores (with pore sizes >50 μm), which limits the electrical conductivity.

Another strategy for obtaining smaller pore sizes is the salt leaching technique, followed by drying. It has been used by Kroon *et al.* to introduce porosity to poly(3-hexylthiophene) (P3HT), resulting in foams with 66% porosity (with pore sizes $\sim$14 μm interconnected with nanopores of 63 nm). Doping by immersion in 2,3,5,6-tetrafluoro-7,7,8,8-tetracyano-quinodimethane (F_4TCNQ)/acetonitrile solution resulted in a comparable *ZT* value (1.8×10^{-4}) to that for P3HT films.[21]

Supercritical drying has been demonstrated as an efficient method to produce a mesoporous (pore sizes <50 nm) 3D network with minimum structure shrinkage and a good compromise between low thermal conductivity and sustained electrical conductivity.[22–24] A relatively high power output of 2 μW was obtained for a temperature difference of 36.5 K on a single PEDOT:PSS aerogel (mesoporous and with a fibrillar structure).[22] Fabricating porous conducting polymers for TE applications is therefore possible, but often the tradeoff between σ, S, and κ is difficult to optimize (as in the case of thin films). Poor mechanical strength can also be a limitation of the porous structure for use in final device applications.

An often-overlooked approach, due to its complexity, consists of polymer blending, either to optimize the TE properties or to improve the mechanical strength of the network. Blending two organic semiconductors, chosen for their compatible density of states, can lead to high Seebeck coefficients.[25] Combining semiconducting polymers with insulating (and thermoplastic) polymers not only reduces the effective cost, but also enhances the mechanical properties. In some cases, the addition of an appropriate insulating polymer can lead to an improvement of the electrical conductivity.[26,27] However, improved thermoelectric performance of conjugated polymers when using an insulating matrix has rarely been reported. An intriguing work by Okada *et al.*[28] highlights that the combination of P3HT and polystyrene nanofibers and high air content leads to a giant Seebeck coefficient (>10 mV K^{-1}). However, their P3HT:PS cryogels (freeze-dried) are brittle and doped with an unstable dopant (*i.e.* iodine vapor) leading to $\sigma = 8 \times 10^{-5}$ S cm^{-1}. The same research team attempted to enhance the mechanical properties by replacing polystyrene with polyurethane (foam-like structure), but the low content of P3HT resulted in poor electrical conductivity.[29]

Zhang *et al.* demonstrated that a cellulose nanofiber skeleton mixed with (3-glycidyloxypropoyl) trimethoxysilane can provide elastic structures with pore sizes between 10 and 100 μm (after freeze-drying). Mixing this porous skeleton with PBFDO or PEDOT:PSS yielded n-type and p-type thermoelectric and elastic aerogels.[30] A maximum power of 1 μW was produced at a temperature difference of 50 K by connecting 12 legs of these aerogels to form a TE module. The work of K. Liu and co-workers is another example of a synergic combination of properties between n-type doped conjugated polymers and insulating elastomers.[31] Uniform bulk nanophase separation between the elastomer (itaconate-butadiene rubber) and the conjugated polymer (P(TDPP-BT-LEG)) leads to an improved elasticity (90% elastic recovery rate beyond 100% strain) and a decrease in thermal conductivity of 50% as compared to the doped semi-conducting polymer. The *ZT* values of the composites exceeded twice those of the pristine polymers, achieving a peak *ZT* value of 0.49 at 300 K. Elastic TE generators achieved maximum power outputs of 229 nW at ΔT = 48 K.

Inspired by our previous work on fibrillar and mesoporous p-[22] and n-type[23] aerogels, for which the 3D structure of the gels was maintained through supercritical drying, and by the work of Okada *et al.*,[28] we propose a new strategy combining both the control of the porous structure (3D fibrillar network) and the use of semi-conducting/insulating polymer blends. P3HT is chosen as the semi-conducting polymer and thermoelectric model material. Syndiotactic polystyrene (sPS) is selected as the insulating polymer for its semi-crystalline character and its ability to form fibrillar gels in a wide variety of organic solvents, as well as self-assembled structures with polyalkylthiophenes.[32]

Specifically, we investigate binary aerogels of P3HT and syndiotactic polystyrene (sPS) in a 1 : 1 weight ratio, fabricated through doping of the gels (immersed in a solution of the dopant in acetone), followed by supercritical drying. A gradual approach is chosen. First, the effect of F_4TCNQ solution concentration on the thermoelectric performances is investigated by assessing morphology and structure–property relationships. The intercalation of the F_4TCNQ dopant molecules into the crystalline phase of P3HT yields similar results to those previously observed in thin films. Then, it is demonstrated that a similar doping and drying protocol can be applied to other dopants without impacting the aerogel's structure. However, in the case of more oxidative dopants, such as $FeCl_3$, the TE properties are further improved. Finally, we demonstrate the feasibility of these materials in application by evaluating the power output of a single-leg device at room temperature, achieving a few tens of nanowatts at 11 K temperature difference.

Experimental

Materials

Poly(3-hexylthiophene-2,5-diyl) (P3HT, average M_w = 60 156 g mol^{-1}, $Đ$ = 2.1, 97.6% RR), syndiotactic polystyrene sPS (M_w = 179.000 g mol^{-1}; $Đ$ = 3.08), 2,3,5,6-tetrafluoro-7,7,8,8-tetracyanoquinodimethane (F_4TCNQ), iron(III) chloride ($FeCl_3$), *p*-xylene, and anhydrous acetone were purchased from commercial suppliers and used as received. Liquid CO_2 and liquid ethane were obtained from Linde. The silver paste was purchased from Agar Scientific (AGG3691).

Gel and aerogel preparation

The fabrication of the gels and aerogels is illustrated in Fig. 1.

For the polymer blend, the rational choice of P3HT : sPS blend content of 0.5 : 0.5 weight fraction is discussed in the SI.

P3HT, sPS and P3HT:sPS gel fabrication. For the preparation of the gels, a weighted amount (between 80 and 100 mg) of the polymer is introduced into a flat bottom Pyrex tube (inner diameter 25 mm) with an SVL screwcap, to which *p*-xylene is added to obtain a final polymer concentration of 6 wt%. The polymer solution is heated at a temperature of 135 °C in an oil bath, under stirring for four hours to ensure complete dissolution (and homogenous mixing of the polymer chains in the case of the blend). After four hours, the heater of the oil bath is turned off, the magnetic stirring bar is removed, and the solution is allowed to reach room temperature (at a cooling rate ∼1 °C min^{-1}). Gels (in the cylindrical shape of the Pyrex tube, with no apparent supernatant, nor volume shrinkage) are formed after crossing the gelation temperature of the polymer (T_{gelation} of P3HT ∼ 31 °C; sPS ∼ 54 °C; P3HT:sPS ∼ 51 °C). The *p*-xylene gels are aged for approximately 36 hours. An orthogonal solvent of the polymers, fully miscible with *p*-xylene and compatible with the supercritical drying process (fully miscible with liquid CO_2) is needed for the next step. Anhydrous acetone is chosen for this purpose and exchanged with *p*-xylene. 40 mL of acetone is slowly added to the tube, left for 12 hours, and then removed. This process is repeated four times in a lap of 48 hours, to exchange the pre-existing *p*-xylene from the gels fully. No change of color, nor gel shrinkage, is observed during the solvent exchanges. The gels are strong enough to be manipulated with a spatula.

Sequential solution doping of the gels. F_4TCNQ doping solutions, of various concentrations ranging from 0.1 g L^{-1} to 2 g L^{-1}, are prepared by dissolving the dopant in anhydrous acetone at room temperature. The solutions are then purged with argon for 15 minutes to remove any remaining oxygen (allowing the doping process to be performed out of the glovebox). The gels are then doped by fully submerging them in the doping solution for 12 hours. UV-Vis absorption spectroscopy measurements showed that the dopant is stable in the solvent under such conditions, see Fig. S3 in the SI. A change in colour (from pink/violet to dark blue) of the gels is observed after only a few minutes of contact with the doping solution, providing visual proof of doping. After this, the doping solution is replaced with a fresh one and the gels are left in it for an additional 12 hours. A shorter doping time could have been used, but the doping kinetic study was not within the scope of this work. Similarly, the gels are doped with 2 g L^{-1} of $FeCl_3$ or F_4TCNQ : $FeCl_3$ (1 : 1.7 molar ratio). The concentrations of the $FeCl_3$ and mixture dopant solutions are selected in order to achieve a maximum electrical conductivity. The doped samples

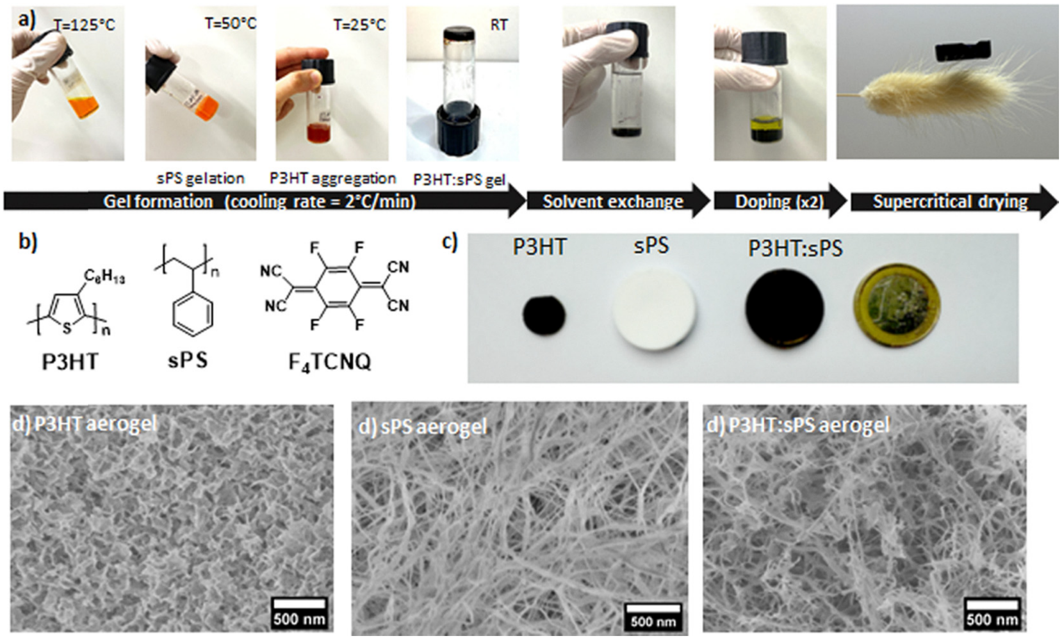

Fig. 1 (a) Flow chart of the gel and aerogel preparation method. (b) Chemical structures of the different components. (c) Images of the final P3HT, sPS, and P3HT:sPS aerogels all prepared from the same volume and a 6 wt% *p*-xylene solution. (d) SEM images revealing the inner structure of the sPS, P3HT, and P3HT:sPS aerogels.

are removed from the dopant solution, without further washing, and then subjected to supercritical drying.

Supercritical drying (SCD) with CO_2. Supercritical drying is done with an SFT-110 supercritical fluid extractor. The gel is loaded, with a splash of acetone, into a 100 mL capacity autoclave, which is then sealed. Initially, the autoclave is supplied with CO_2 in the liquid phase (4 °C, 750 psi in the bottle). The temperature in the autoclave is maintained at 20 °C, and the pressure at 1200 psi. The gel, in the autoclave, is immersed in liquid CO_2 for 30 min, and then the liquid CO_2 is half-drained (50 mL) and flushed with fresh one from the CO_2 bottle. This solvent exchange (from acetone to liquid CO_2) is repeated five times in 30-minute intervals to replace acetone with liquid CO_2 in the gel completely. Then, the autoclave (at 1200 psi) is heated to 45 °C for 1.5 h, to induce the transition of CO_2 from the liquid to the supercritical phase. Then, the outlet valve is slightly opened to create a dynamic flow inside the autoclave, allowing supercritical CO_2 to flow through the gel. The sample is kept under these conditions (45 °C and 1200 psi) for 30 min, followed by slow release of pressure while keeping the temperature constant. After complete venting (approx. 20 min), the sample is transferred to a vial and degassed for a few minutes in the antechamber of the glove box. The aerogels are stored in a glove box under an inert atmosphere with oxygen and moisture levels below 5 ppm.

Characterization

The apparent density of the aerogel is calculated by dividing the sample weight by the volume, $\rho = \frac{m}{v}$. On average, the samples are 22–24 mm in diameter and 3–4 mm thick (see Fig. 1c).

Then, the porosity is determined from the density values using the following equation:

$$\%\ \text{Porosity} = \left(1 - \frac{\text{Aerogel density}}{\text{density(sPS)} \times (1-r) + \text{density(P3HT)} \times r}\right) \times 100 \tag{1}$$

where ρ(sPS) = 1.04 g cm^{-3},[33] ρ(P3HT) = 1.10 g cm^{-3},[34] and r is the wt% of the P3HT, in this case, r = 0.5. The densities and porosities of the samples are given in Table 1.

Nitrogen physisorption

Textural characterization is done using a Micromeritics ASAP 2420 apparatus by determining nitrogen physisorption isotherms at 77 K. The aerogel sample is cut into small pieces and loaded into an analysis tube. Before adsorption measurements, the sample is outgassed at room temperature for 5 hours under vacuum to remove the moisture from the aerogel. The specific surface area (S_{BET}) is calculated according to the criteria provided in the literature,[35,36] and by using the Brunauer–Emmett–Teller (BET) method applied in the $0.05 \leq p/p^0 \leq 0.30$ ranges.

Differential scanning calorimetry (DSC) measurements are performed using a DSC 8500 from PerkinElmer under nitrogen gas flow. Samples, placed in a stainless steel pan, are heated from 25 °C to 280 °C at a rate of 5 °C min^{-1} and then cooled to room temperature at the same rate. Only the first cycle was considered, as it is more representative of the aerogel's thermal history.

The degree of crystallinity χ_c is evaluated using $\chi_c = \Delta H_f/\Delta H_f^\circ$ with $\Delta H_f^\circ = 33$ J g^{-1} the melting enthalpy for a 100% crystalline sample of P3HT[37] and $\Delta H_f = 53.2$ J g^{-1} the melting enthalpy for a 100% crystalline sample of sPS.[38] In the blend, the melting enthalpy is weighted by r and $1 - r$, respectively, giving $\Delta H_f = 43.1$ J g^{-1} the melting enthalpy for a 100% crystalline sample of P3HT : sPS (0.5 : 0.5).

Compressive tests are performed using an electrodynamic tensile/compressive machine (Instron ElectroPuls E3000) under ambient conditions. The measurements are repeated on three samples, and the average Young's modulus is determined.

Scanning electron microscopy (SEM) is used to examine the morphologies and porous structures of various samples. The measurements are performed using a FEG-cryo-SEM (Hitachi SU8010) operating at an accelerating voltage of 1 kV at room temperature.

Cryo-SEM. A small piece of gel in *p*-xylene was sliced off with a razor blade, quickly dipped into slush nitrogen and then transferred under high vacuum (10^{-6} mbar) and low temperature (−150 °C) into the Quorum PT 3010 chamber attached to the microscope. There, the frozen sample is fractured with an adapted razor blade and etched (*via* a slight sublimation) at −70 °C to reveal the details of the morphology. The sample is then transferred into the FEG-cryo-SEM (Hitachi SU8010) and observed at 1 kV at −150 °C (under 10^{-6} mbar).

SEM-EDX. Elemental mapping is carried out by energy dispersive X-ray spectroscopy (EDX) analysis. Backscattering electron images are obtained using the "in-chamber" dedicated backscattered electron detector of a Zeiss Gemini SEM 500 microscope at 5 kV. A vertical cross-sectional cut of the sample is prepared and mounted on a sample holder. SEM-EDX measurements are then carried out at multiple locations from the top to the bottom, including the central region, to assess the dopant distribution throughout the sample.

Wide angle X-ray scattering measurements (WAXS) on undoped and doped samples (Fig. 2 and Fig. S11) are performed at the *Dfféri*X platform of the Institut Charles Sadron

Table 1 Structural and thermal characterization studies of neat and composite aerogels (prior to doping)

Non doped aerogel	Density (g cm^{-3})	Porosity (%)	Melting temperature (°C)		ΔH_m (J g^{-1})		Degree of crystallinity (%)		
P3HT	0.21	80	247		26		79		
P3HT:sPS	0.07	93	P3HT	sPS	P3HT	sPS	P3HT	sPS	P3HT:sPS
			242	274	4.3	11.2	13	21	36
sPS	0.03	95	275		25.3		48		

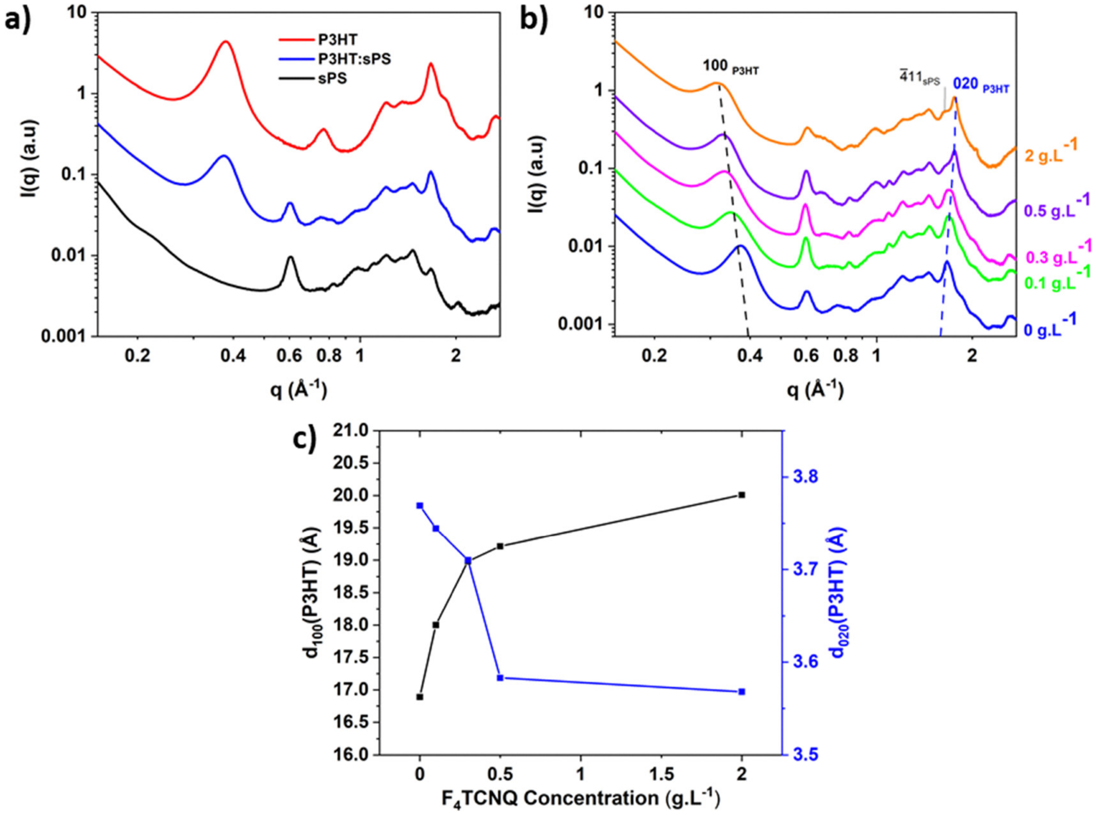

Fig. 2 (a) WAXS intensity profiles as a function of the scattering vector q for P3HT aerogel (red), sPS aerogel (black), and P3HT:sPS aerogel (blue). (b) WAXS intensity profiles as a function of the q vector of pristine and doped P3HT:sPS aerogels. The F_4TCNQ dopant concentration in acetone was varied between 0.1 and 2 g L^{-1}. (c) Evolution of the d_{100} alkyl layer spacing and the d_{020} π-stacking period of the crystalline phase of P3HT as a function of the dopant concentration.

using two diffractometers installed on a Rigaku rotating anode (MicromaxTM-007 HF, operating power 40 kV – 30 mA). The collimated monochromatic beam (Cu-Kα radiation, wavelength λ = 0.154 nm) was obtained using a confocal multilayer mirror (Max-Flux OpticsTM, Osmics, Inc.) and a pinhole system. The scattered intensity is collected either on a Pilatus 3R 300 K camera (Dectris Ltd., Switzerland) at 20 cm downstream of the sample (transmission mode), or on Fuji imaging plates at 10 cm, covering scattering angles from 2θ = 0.6 to 44° and a scattering vector range from q = 0.04 to 3 Å^{-1} (with $q = 4\pi\sin(\theta)/\lambda$).

Complementary measurements on $F_4TCNQ\text{-}FeCl_3$ doped samples were performed on a XEUSS Pro HR diffractometer (Xenocs, France) equipped with a GeniX 3D Cu HF VL microfocus source (50 kV, 0.6 mA, λ = 0.154 nm). A monochromatic and collimated beam was obtained using a FOX3D single-reflection multilayer optic combined with scatterless slit modules. The scattered intensity was collected with an EIGER2 R 1M detector (Dectris Ltd, Switzerland, beamstop-free mode) positioned 10 cm from the sample, providing a q-range of 0.04–2.3 Å^{-1}.

Electrical conductivity. The electrical resistance is measured using a standard collinear four-probe method with a probe space of 1.6 mm. The electrical resistivity and conductivity are calculated using the following equation extracted from Serdar Yilmaz's geometrical factor report:[39]

$$\rho = \frac{1}{\sigma} = G \cdot \frac{V}{I}, \tag{2}$$

and

$$G = 2\pi s \times F_1\left(\frac{t}{s}\right) \times F_2\left(\frac{d}{s}\right) \tag{3}$$

where ρ is the electrical resistivity, σ the electrical conductivity, V the voltage, I the current intensity, s the probe space (1.6 mm), t the sample thickness, d the sample diameter and $F_1\left(\frac{t}{s}\right)$ and $F_2\left(\frac{d}{s}\right)$ are correctional factors for the thick circular sample of finite thickness (with $t > 2s \sim 3.2$ mm).

The experiment was performed on two aerogels, and the measurements were repeated four times on each sample.

Seebeck coefficient. The Seebeck coefficient is measured using a differential temperature method. A homemade setup consisting of one heating and one cooling Peltier cell allows an in-plane controllable temperature gradient. Measurements are performed by gradually increasing the temperature difference between the two Peltier cells up to 12.8 K (starting from 293 K, the midpoint temperature). For each temperature step, the tension is measured five times with a 20 s interval (see the previous report[40] for a description of the setup). To ensure good thermal contact between the Peltier cells and the aerogels, copper legs (1 × 1 × 0.2 mm) are affixed to the bottom of the sample with conducting silver paste. The thermovoltage is measured directly on the silver paste. The experiment is performed on two aerogels.

Cross-plane measurements. Cross-plane Seebeck coefficients and output power are measured with a homemade setup, where the samples are sandwiched between hot and cold copper disks 1 cm in diameter.[41,42] To ensure good electrical and thermal contact with the sample, a minimum slight pressure is applied to each sample using a torque screwdriver (tightening torque = 0.3 N m^{-1}). Using Peltier modules as heating and cooling sources and thermocouples embedded inside each copper disk, a temperature gradient is then imposed and measured across the two sides of the samples. An external cooling flow system, aided by a cryostat, is used to maintain a uniform thermal gradient across the sample thickness. The operating temperature is set at 293 K, while the maximum thermal gradient is fixed at 11 K. The system allows measuring the potential difference ΔU and the temperature difference ΔT, giving the Seebeck coefficient α from the slope $\Delta U/\Delta T$ of the voltage–temperature curve. Considering the sample as a thermoelectric generator, the output power is determined as a function of an adjustable external load circuit. When the output power is at its maximum, the load resistance is equal to the internal resistance of the sample.

The thermal conductivity of the aerogels is measured using the transient plane source (TPS) technique by utilizing a commercial apparatus (Hot Disk®, TPS 1000) as described in a previous report.[22]

The experiments are performed under ambient conditions. The input power and time duration are set at 5 mW and 20 or 40 s. The measurements are repeated four to five times, with 30 min stabilization between each measurement.

Results and discussion

Fabrication of the aerogels

Aerogels are formed in two steps: first, by polymer gelation in a solvent, inducing the formation of a 3D network, followed by solvent extraction under supercritical conditions (see Fig. 1a and experimental part). sPS is known to form a fibrillar thermoreversible gel in *p*-xylene at 45 °C.[43] P3HT forms whisker-like nanofibers in the same solvent but at a lower gelation temperature (between 26 and 34 °C).[44,45] The polymer gels with r = 0, 0.5 and 1 are prepared by thermally induced phase separation (TIPS) during the gradual cooling of the polymer solution in *p*-xylene from 135 °C to room temperature. Cryo-SEM confirms the fibrillar nature of P3HT:sPS gels in their *p*-xylene native solvent (see the SI, Fig. S2). For the P3HT : sPS blend (0.5 : 0.5), the orange solution (at elevated temperature) undergoes a gradual transition to a reddish, viscous solution, which then gels and darkens to a deep brown after 36 hours at room temperature (see Fig. 1a). These color changes suggest P3HT aggregates, but also that possible interactions between sPS and P3HT take place. Spectroscopic evidence of the aggregation phenomenon, inducing a change in color, was indeed observed by Samanta *et al.* in a similar system (0.5 : 0.5 P3HT : PS in *p*-xylene, but at a low polymer concentration).[32]

The gels are then subjected to supercritical drying (SCD) with CO_2 to produce aerogels with minimized shrinkage and structural distortion. SCD prevents the collapse of the gel's porous structure caused by capillary forces[22] and avoids the mechanical stress imposed by the freeze-drying method, which often results in a cracked and fragile structure (as was the case with the P3HT:PS composites prepared by Okada *et al.*).[28]

As the gel initially contained *p*-xylene (immiscible with liquid CO_2), this solvent was first replaced by acetone (fully miscible with *p*-xylene and liquid CO_2, and a non-solvent of both polymers), followed by an exchange with liquid CO_2 (at higher pressure) before reaching the supercritical conditions of CO_2.

After drying, a dark purple, robust, and lightweight (0.07 g cm^{-3}, 95% porosity) P3HT:sPS aerogel is obtained (see Fig. 1a and Table 1). A slight volume shrinkage of 10–20% is observed compared to the initial shape of the wet gel. For comparison, 100% P3HT and 100% sPS aerogels are also produced (with a similar process: gel formation in 6 wt% *p*-xylene followed by solvent exchange with acetone and drying under supercritical conditions with CO_2). While the sPS aerogel also exhibits a low density of 0.03 g cm^{-3} and a slight shrinkage, pristine P3HT yields a significantly denser aerogel (0.23 g cm^{-3}) and a shrinkage of 80% as compared to its gel state. This is likely due to the drying conditions, particularly the temperature of 41 °C (needed to reach the supercritical state of CO_2), which exceeds the sol–gel transition temperature of 26 °C of P3HT.[44] This probably disrupts the preformed three-dimensional structure of the P3HT thermoreversible gel, resulting in substantial shrinkage of the final aerogel (as illustrated in Fig. 1c). Furthermore, the P3HT aerogel is very brittle and breaks easily while being manipulated (limiting its TE property measurements and its potential use in a TE generator). The P3HT:sPS aerogels are handleable with tweezers and exhibit an average Young's modulus of 0.53 MPa under compression (see the SI, Fig. S4), compatible with their use in device applications. This value is in the same range as the one found for the δ form of the sPS aerogel (96% porosity).[46] Blending sPS with P3HT, combined with the supercritical drying method, is therefore an interesting strategy to enhance the mechanical strength of the final aerogel.

The porosity of the P3HT:sPS aerogels is evaluated using the nitrogen physisorption technique. The average specific surface area is found to be $S_{BET} = 382 \pm 130$ m^2 g^{-1} and the average mesopore volume of $V_{mesopores} = 0.61 \pm 0.13$ cm^3 g^{-1} (see the SI, Fig. S5). We find a broad mesopore size distribution, ranging from ∼2 to ∼50 nm with a majority population at 5 nm. A minor fraction of macropores (>50 nm) is also present (as seen in SEM images), but nitrogen physisorption is not well adapted to probe such large pore sizes. The slight initial rise in the curve (at $p/p^0 < 0.05$) is associated with micropore filling (but this concerns a minor fraction of pores, described in the SI).

The SEM images of the blend aerogel (Fig. 1d) depict a fibrillar network that combines long fibers with denser connection points, forming a 3D porous network. The average diameter of the thinner fibers is measured at $d_{\mathrm{P3HT:sPS}} = 18 \pm 5$ nm. The voids between the fibers are in the range of a few tens of nanometers (consistent with the nitrogen physisorption results). The technique does not allow the distinction between P3HT and sPS in the blend (as it is insensitive to chemical/electronic contrast).

The structural agreement between cryo-SEM and SEM images provides strong evidence for the preservation of the native gel architecture formed in *p*-xylene, which persists through both the solvent exchange and drying processes. These imaging techniques suggest that the aerogel preparation method effectively maintains the original structural characteristics of the gel network.

As seen in DSC, the aerogels are semi-crystalline with a crystalline fraction of 13% for P3HT and 21% for sPS (see the SI, Fig. S6, and Table 1).

In the 0.5 : 0.5 blend, the expected degree of crystallinity would be 24% for sPS and 39.5% for P3HT, assuming a similar degree of crystallinity to that of the 100% polymer aerogels, weighted by *r*.

The crystalline fraction of P3HT observed in the blend is much lower than that in 100% P3HT (13% compared to 79 × 0.5 = 39.5%), whereas the sPS crystallinity degree is in a similar range (21% compared to 48 × 0.5 = 24%). Upon cooling, sPS crystallizes at 235 °C, while P3HT crystallizes at a lower temperature of 197 °C. The crystallization temperatures in the blend aerogel are 274 °C for sPS and 242 °C for P3HT. These results suggest that in the gel state, the formation of the sPS network occurs before that of P3HT, creating an sPS matrix for P3HT, before the actual crystallization of the latter and limiting this process. There is no experimental evidence that sPS acts as a nucleating agent for P3HT.

Investigation on the homogeneity of the dopant distribution within the aerogel

To make the aerogels conductive, 2,3,5,6-tetrafluoro-7,7,8,8-tetracyanoquinodimethane (F_4TCNQ) is first used as the electron-accepting dopant for P3HT. The P3HT:sPS blend is doped with F_4TCNQ in the gel state (before drying, to preserve the porous structure) during the solvent exchange steps in acetone (see the experimental part and Fig. 1a). Different dopant solution concentrations are investigated (from 0.1 to 2 g L^{-1} in acetone). A maximum dopant diffusion/doping level was aimed for and was obtained after two immersions of the gels in the doping solution (see Fig. S3b in the SI). A change of color from violet to dark blue is observed in the gel state upon doping (which can be correlated with the typical polaronic band emerging from the ion pair formation and the electron transfer from the polymer to the dopant).[11] The dark blue color is maintained after drying.

Cross-sectional SEM imaging of the doped samples, coupled with energy-filtered dispersive X-ray spectroscopy (EDX), is used to visualize the distribution of dopant molecules throughout the sample thickness (SI, Fig. S7 and S8). SEM-EDX imaging of the doped sample is performed at multiple points along the sample height. P3HT (identified by the sulfur atom) is well dispersed within the aerogel. The consistent detection of fluorine signals (originating from the F_4TCNQ molecules), on both the aerogel surfaces and within the sample core, indicates efficient diffusion of F_4TCNQ throughout the porous structure across the sample thickness of 4 mm. No evidence of phase separation (between non-doped amorphous P3HT phase, non-doped sPS and doped crystalline phase) can be visualized. This indicates that P3HT and sPS are well intermixed, since the fluorine atoms are homogeneously distributed.

The exact amount of F_4TCNQ in the polymer matrix is difficult to estimate with EDX due to the uncertainty of the probed depth (because of the roughness and the porosity of the sample).

Nevertheless, porosity allows for efficient dopant diffusion through a thickness of 3–4 mm, as opposed to dense cubic P3HT samples, where only 250 μm were found to be doped after 14 hours of sequential doping.[47]

Structural analysis of the doped aerogels

WAXS intensity profiles of the neat polymer aerogels and of the blend are shown in Fig. 2a. For P3HT, the typical *h*00 (*h* = 1–2, at 0.38 and 0.76 $\mathrm{\AA}^{-1}$) scattering peaks due to the lamellar stacking as well as the 020 peak (at 1.67 $\mathrm{\AA}^{-1}$) of the π-stacking are observed.[48,49]

Syndiotactic polystyrene (sPS) exhibits four distinct crystal structures (α, β, γ, and δ), along with intermediate forms with different molecular conformations. The polymorphism of sPS is complex, with α and β crystalline phases having a planar zigzag all-*trans* chain conformation (T_4), and γ and δ polymorphs showing a closely packed helical T_2G_2 chain.[50,51] The absence of 110 and 020 peaks at respectively $q = 0.48$ and 0.43 $\mathrm{\AA}^{-1}$ is evidence of not having an α or β form of sPS but rather a helical structure with T_2G_2 conformation.[52] The characteristic peaks at *q* values of 0.6, 0.96, 1.21, 1.46, and 1.67 $\mathrm{\AA}^{-1}$ coincide with the main peaks of the δ (δe) form. This particular δe form has been described as a result of a co-crystal between the solvent and the sPS, leaving behind empty nano-porous cavities after complete solvent removal.[53,54] The presence of a signal at $0.02 \le p/p^0$ in the nitrogen physisorption curves is consistent with a minor fraction of microporosity (pore size <2 nm) in the sample. This could be attributed to the presence of the nano-cavities in the δe form of sPS.

The WAXS intensity profile of the blend aerogel (in blue, Fig. 2a) shows the characteristics of both the crystalline phase of P3HT and the δ form of sPS. No new peak or significant shift in the peaks is observed, indicating the absence of co-crystal formation or a particular crystalline interaction between the two polymers. Upon doping with F_4TCNQ at different concentrations (Fig. 2b), a shift of the *h*00 P3HT scattering peaks to lower *q* values and a shift of the 020 P3HT peak to higher *q* values are observed. The shifts are continuous. The increase in the lamellar distance and the decrease in the π-stacking distance of P3HT (Fig. 2c) are known phenomena in doped thin films, and have been ascribed to the intercalation of F_4TCNQ molecules between the alkyl side chains of the crystalline phase of P3HT.[40]

A maximum of $d_{100} = 20.01$ Å ($d_{100} = 2\pi/q_{100}$) and a minimum $d_{020} = 3.57$ Å ($d_{020} = 2\pi/q_{020}$) are obtained with a concentration of 2 g L^{-1} of the F_4TCNQ dopant solution. It was not possible to increase further the concentration of the dopant due to solubility limitations in the solvent. Nevertheless, a maximum dopant intercalation into the crystalline structure has been reached (as also confirmed by the plateau reached in the electrical conductivity and the Seebeck coefficient at high concentration). The variation of the unit cell of P3HT upon doping the aerogels follows the variation observed in highly crystalline rubbed thin films. Still, the unit cell volume is much higher for the aerogels. Interestingly, at saturation (maximum electrical conductivity), the layer spacing of the doped fibrillar aerogel reaches a higher value (20 Å) than that of rubbed thin films (17.9 Å).[55]

We conclude that the dopant molecules diffuse well into the fiber-like structure of the aerogel, intercalating within the lamellar structure of P3HT. The peaks attributed to the δ form of sPS do not change upon doping (neither in position nor in intensity). Therefore, the F_4TCNQ molecules do not disturb the crystalline structure of sPS. No crystalline phase of F_4TCNQ is seen in the WAXS patterns of the doped aerogels (see the WAXS pattern of F_4TCNQ crystalline powder, Fig. S11b, SI).

As also seen in the electrical conductivity measurement, the solvent exchange with liquid CO_2 and supercritical drying does not affect or wash out the F_4TCNQ molecules from the gels. We assess that the aerogels contain a high fraction (∼37% according to DSC) of amorphous P3HT. We cannot comment on whether those amorphous phases are partially doped, due to the lack of an analytical method suitable for these mm-thick and porous materials.

Thermoelectric properties of the composite aerogels doped with F_4TCNQ

The electrical and thermal conductivities and the Seebeck coefficient of the aerogels are measured using the method we have developed for porous conducting polymers and described in ref. 22.

Fig. 3 illustrates the evolution of the thermoelectric properties of the P3HT:sPS aerogel as a function of the doping solution concentration. The non-doped aerogels feature a low electrical conductivity (2×10^{-6} S cm^{-1}) but a high Seebeck coefficient (877.8 μV K^{-1}).

A significant increase of the electrical conductivity (more than three orders of magnitude) is obtained at a low concentration of the dopant of 0.1 g L^{-1}. The electrical conductivity then reaches a plateau at a concentration of 0.5 g L^{-1}, and a maximum value of 4.6×10^{-2} S cm^{-1} for a concentration of 1 g L^{-1}. These values correspond to the apparent electrical conductivities of the aerogels, which include the contribution of approximately 95% of air and a sPS insulator content of 50 wt%.

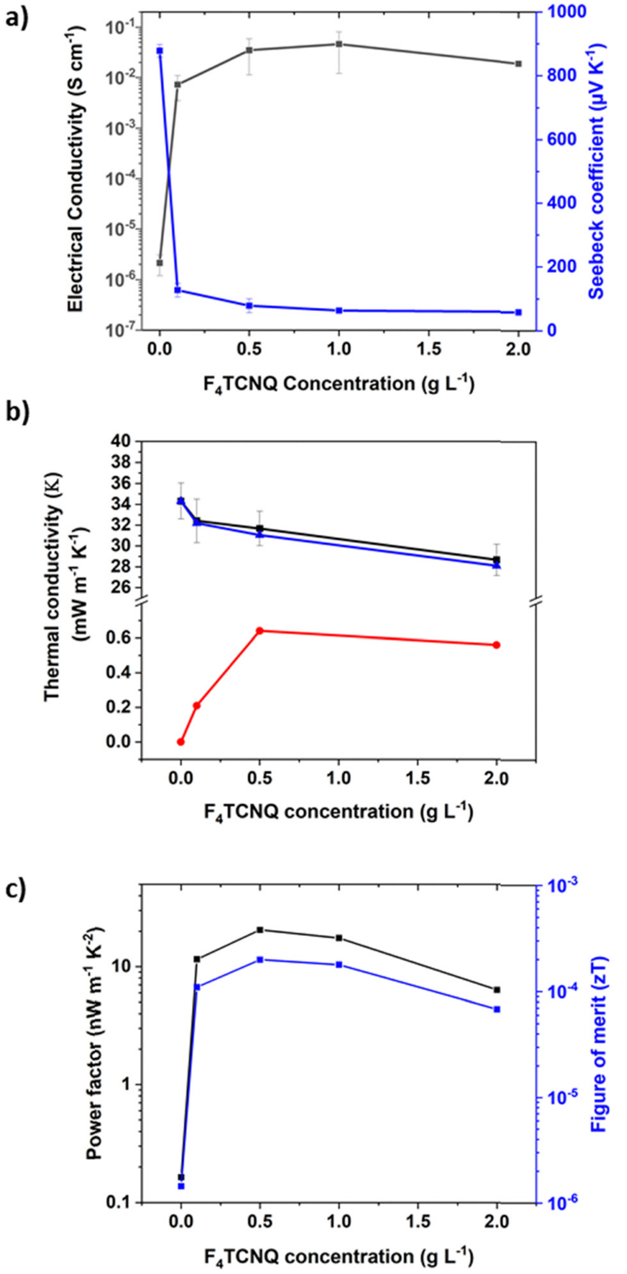

Fig. 3 Evolution of the thermoelectric properties as a function of the F_4TCNQ concentration in acetone of the P3HT:sPS aerogels: (a) electrical conductivity (in black) and Seebeck coefficient (in blue). (b) Total thermal conductivity (in black) and its components (the lattice contribution in blue and the electronic contribution in red). (c) Power factor (in black) and figure of merit ZT (in blue) calculated at 300 K.

To compare with a dense material, we can use a theoretical model to estimate the electrical conductivity (σ_0) considering the volume fraction of the pores and the pore geometry (for open-cell porous materials). The one developed by Ashby *et al.*[56] follows eqn (4):

$$\sigma_0 = \frac{\sigma_{\text{porous}}}{\frac{1}{3}\left[(1-\Theta) + 2(1-\Theta)^{\frac{3}{2}}\right]} \tag{4}$$

where σ_{porous} is the apparent electrical conductivity measured on the porous material, and Θ the porosity of the material (*e.g.* 0.95, for the 0.5 : 0.5 P3HT : sPS aerogel). The σ_0 value (~2 S cm^{-1}, for 1 g L^{-1}) is close to the standard values of P3HT doped with F_4TCNQ in thin films,[57] although 50 wt% of the solid content of the aerogel is isolating (sPS). We can therefore conclude that the doping of the aerogel is quite efficient, and that a maximum doping level has been reached (as shown by the plateau of the electrical conductivity).

Concurrently, S decreases from 877 to 58 μV K^{-1}, with a plateau reached at 0.5 g L^{-1}. The low Seebeck values achieved are similar to those obtained for a relatively highly doped P3HT film with F_4TCNQ,[40,55] also indicative of effective doping in the aerogel. As opposed to the claims of Okada *et al.*,[28] there is no experimental evidence that either the fibrillar structure or the presence of sPS plays a role in the Seebeck coefficient, since the values obtained for P3HT:sPS are similar to those reported in the literature for P3HT.

The Seebeck coefficient and the electrical conductivity follow the empirical relationship $S \sim \sigma^{-1/4}$ proposed by Glaudell *et al.*[58] and observed for similar P3HT foam and solid samples[21] (see the SI, Fig. S9).

At a dopant concentration of 0.5 g L^{-1}, the P3HT:sPS aerogel achieves an electrical conductivity of 3.5×10^{-2} S cm^{-1} and a Seebeck coefficient of 76.8 μV K^{-1}, resulting in a maximum PF of 2×10^{-2} μW m^{-1} K^{-2}.

The transient plane source method is used to measure the thermal conductivity of the aerogels. The undoped polymer blend aerogel exhibits a low thermal conductivity of 34 ± 1 mW m^{-1} K^{-1}, attributable to its very low density and fibrous structure. The thermal conductivity of the sPS aerogel (35 mW m^{-1} K^{-1}) is similar to that of the undoped P3HT:sPS sample. The thermal conductivity of P3HT aerogels could not be measured using the TPS method due to geometrical constraints of the shrunken P3HT sample.

By increasing the dopant concentration in solution (and the doping level of the final aerogel), the thermal conductivity decreases further, reaching a record low value (as compared to the state of the art on conducting polymers) of 29 ± 1 mW m^{-1} K^{-1} for the sample doped at 2 g L^{-1} in acetone. A discussion on the possible origin of this effect is provided in the SI.

Nevertheless, the impact of F_4TCNQ on κ is less significant than on the electrical conductivity and the Seebeck coefficient. The evolution of *ZT* (calculated at 300 K, shown in Fig. 3c), follows the evolution of the power factor as a function of the dopant concentration, with a maximum obtained at 2×10^{-4} for a dopant concentration of 0.5 g L^{-1}. Thus, in such a highly porous material, the thermal conductivity is not a limiting factor for the material's thermoelectric efficiency *ZT*, unlike the electrical conductivity.

Further improvement of TE efficiency by changing the dopant molecule

To increase the electrical conductivity of the aerogel, a more efficient dopant of P3HT can be used.[11] To maintain the preparation method (and the structure) of the aerogels, a dopant stable in acetone and compatible with the gelling and drying processes is required. $FeCl_3$ appears to be the dopant of choice for our system. We used both pure $FeCl_3$ and a mixture of $F_4TCNQ:FeCl_3$ to maximize the doping efficiency of the aerogels. Mixing complementary dopants (*i.e.* molybdenum complexes and $FeCl_3$) has already been proven as an efficient strategy to increase the electrical conductivity of P3HT.[59] But, to the best of our knowledge, the $F_4TCNQ:FeCl_3$ mixture has not yet been reported. We hypothesise that the $F_4TCNQ:FeCl_3$ mixture will dope both the amorphous and the crystalline phase of P3HT. The $F_4TCNQ : FeCl_3$ molar ratio (1 : 1.7) has not been optimized and will be the scope of further studies.

The thermoelectric properties are summarized in Fig. 4a and Table 2.

As compared to the sample doped with F_4TCNQ, the apparent electrical conductivity is increased by 32 and by 52-fold for the aerogels doped, at saturation, respectively with $FeCl_3$ and $F_4TCNQ:FeCl_3$. This demonstrates that the doping at the gel state and the supercritical drying processes are compatible with other dopant molecules. An apparent electrical conductivity of a few S cm^{-1} is achievable in highly porous samples containing

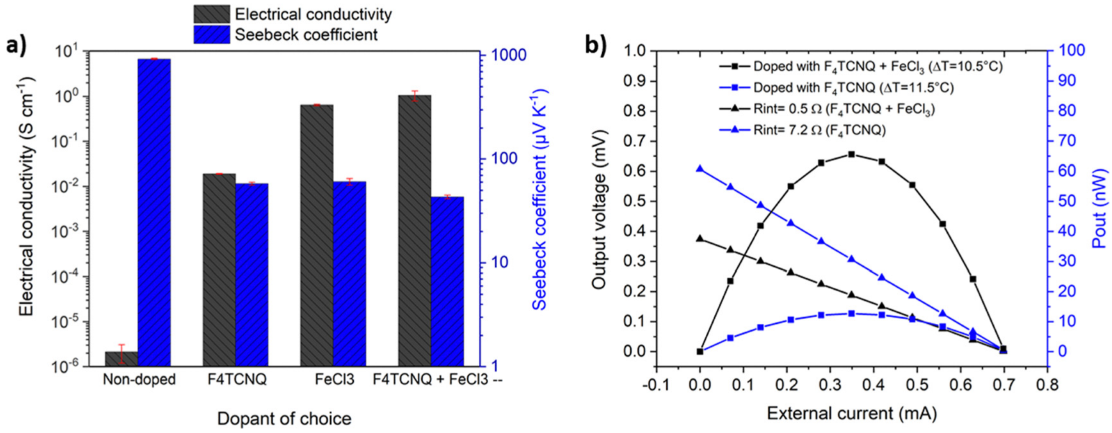

Fig. 4 (a) Electrical conductivity and Seebeck coefficient of P3HT:sPS as a function of dopant nature. (b) Output voltage and output power as a function of current for typical P3HT:sPS aerogels doped with F_4TCNQ or the dopant mixture for a temperature gradient set at 11 K.

Table 2 Thermoelectric properties of the aerogels doped with different dopants (at a similar concentration of 2 g L^{-1}). The mean values are given for two to three samples, with at least two measurements per sample. The output power density is measured on only one sample

P3HT:sPS aerogel doped at 2 g L^{-1}	Porosity (%)	Electrical conductivity (S cm^{-1})	Seebeck coefficient (μV K^{-1})	Power factor (nW m^{-1} K^{-2})	Thermal conductivity (mW m^{-1} K^{-1})	ZT (@300 K)	Output power density at ΔT = 11 K (nW cm^2)
Non-doped	93	$2 \times 10^{-6} \pm 9 \times 10^{-7}$	924 ± 12	0.2	34 ± 1	1.6×10^{-6}	—
F_4TCNQ	95.8	0.02 ± 0.004	58 ± 2	6.4	29 ± 1	6.9×10^{-5}	16.7
$FeCl_3$	91.6	0.64 ± 0.02	61 ± 5	234.3	44 ± 1	1.6×10^{-3}	
F_4TCNQ + $FeCl_3$	96.8	1.05 ± 0.25	43 ± 2	194	30 ± 1	1.9×10^{-3}	83.3

50 wt% insulating material by increasing the doping efficiency. To compare with dense films reported in the literature, the σ_0, calculated with eqn (4), reaches a value of 14.5 and 72.5 S cm^{-1} for the sample doped with $FeCl_3$ and F_4TCNQ:$FeCl_3$, respectively.

$FeCl_3$ (which has strong oxidation capabilities) is also known to dope the amorphous phase of the P3HT[11,59] (which represents a majority fraction in the polymer blend, according to DSC).

The crystalline structure of the samples doped with $FeCl_3$ is similar to that of those doped with F_4TCNQ, as seen in the WAXS intensity profile (SI, Fig. S11a). The lattice parameters of P3HT are also affected by $FeCl_3$ dopant molecules with d_{100} = 19 Å and d_{020} = 3.58 Å. This indicates that $FeCl_3$ dopant molecules may also intercalate within the layers of the alkyl side chain of P3HT. However, the variation of the P3HT unit cell with $FeCl_3$ is less important than with F_4TCNQ. The structure with the mixed dopant is in an intermediate state between those of the $FeCl_3$- and F_4TCNQ-doped samples (see Table S1 in the SI). The increase in electrical conductivity of the aerogels doped with $FeCl_3$ could be attributed to the doping of both amorphous and crystalline phases of P3HT. The combination of $FeCl_3$ and F_4TCNQ results in an even higher electrical conductivity.

To the best of our knowledge, this synergetic combination has never been reported and may be attributed to a higher doping level.

Interestingly, the Seebeck coefficient of the $FeCl_3$-doped aerogel is as high as that of the F_4TCNQ-doped sample. Iron chloride is known to sustain the Seebeck coefficient while increasing the electrical conductivity of the samples. The decrease in the Seebeck coefficient with the use of the mixture of dopants is challenging to analyze.

The thermal conductivity is not affected by the dopant nature and remains at low values below 30–40 mW m^{-1} K^{-1}. The slight increase in the thermal conductivity of the $FeCl_3$-doped sample is related to the slight density variation from sample to sample.

Overall, ZT values of 1.6×10^{-3} and 1.9×10^{-3} are obtained for $FeCl_3$ and F_4TCNQ:$FeCl_3$, respectively, thanks to the important increase in the electrical conductivity as compared to the F_4TCNQ-doped aerogel. These figures of merit are among the highest reported ones for porous polymer systems (see Table S3 in the SI).

Under inert storage conditions in the glove box, the aerogels doped with the three conditions are stable for more than a hundred days (see Table S2 in the SI). This is a promising result for stability, which needs to be considered with other storage conditions.

To evaluate the potential of the P3HT:sPS aerogels for TE applications, the materials were tested as thermoelectric generators with a single vertical pillar. The setup is described in ref. 22 and the experimental part. The output powers are measured in air as a function of an adjustable external load circuit. A low temperature difference of 11 K was applied (with the average temperature at 293 K).

The P3HT:sPS aerogel doped with F_4TCNQ (F_4TCNQ:$FeCl_3$, respectively) shows a maximum power output of 13 nW (65 nW) with an internal resistance of 7.2 Ω (0.95 Ω). The measurement area was 0.78 cm^2, and thus a maximum power output per area is obtained at 16.7 nW cm^{-2} (83.3 nW cm^{-2} for F_4TCNQ:$FeCl_3$). The absolute values of power output must be taken with caution, as only one sample was measured. However, the higher TE properties of the sample doped with the mixture of dopants resulted in higher power output generation (five times higher than the sample doped with F_4TCNQ alone).

The most significant finding is that aerogels can act as thermoelectric generators capable of delivering output powers of a few tens of nW when subjected to moderate temperature differences (approximately 10 K), despite having a low figure of merit. The power output generated by a single aerogel is much higher than that of most organic thermoelectric thin-film devices, which are made up of several legs.[60]

Conclusions

Reproducible P3HT:sPS fibrillar and mesoporous aerogels are fabricated by TIPS, solvent exchange, and supercritical drying with CO_2. sPS brings mechanical strength to the final aerogels. sPS and P3HT fibers are well-intermixed. F_4TCNQ can easily dope the gel and sustain the drying conditions. This method yields robust samples that could be well-characterized. The structural variation of the crystalline lattice of P3HT upon doping follows that of thin films. We assume that F_4TCNQ molecules mainly dope the crystalline phase of the P3HT and intercalate in the lamellar packing of the side chains. By increasing the dopant solution concentration, a saturation of doping is probably reached. A plateau is observed in the variation of electrical conductivity and the Seebeck coefficient with the doping concentration, indicative of a maximum dopant uptake. The limited electrical conductivity measured reflects the high porosity of the aerogel and an optimum porosity are still to be found. A low thermal conductivity record (29 mW m^{-1} K^{-1}) is achieved in this highly porous and conducting polymer system.

The Seebeck coefficient of the doped P3HT:sPS aerogels is close to that achieved for F_4TCNQ-doped P3HT thin films.[57] The giant Seebeck coefficient (> 10 mV K^{-1}) obtained on freeze-dried P3HT:PS by Okada *et al.*[28] was not reproduced with our P3HT:sPS aerogel dried under supercritical conditions (with a similar porosity >95%). Herein, high Seebeck coefficients (> 900 μV K^{-1}) are only obtained for the non-doped aerogel samples. Our results do not support the assumption by Okada and co-workers that porosity, fibrillar structure, and the presence of sPS can enhance the Seebeck coefficient. Despite a fairly low Seebeck coefficient in our case, higher PF and *ZT* were nevertheless obtained for a comparable porous blend based on P3HT and PS. In particular, the $FeCl_3$ dopant and a mixture of $FeCl_3$:F_4TCNQ are a good strategy to further enhance the power factor without compromising the thermal conductivity. We assume that $FeCl_3$ also dopes the amorphous phase of P3HT. The higher figure of merit obtained with the mixture of dopants is reflected in the final output power generated with a thermal gradient of 11 K through the sample.

Producing porous and bulk samples helps maintain a small thermal difference throughout the sample. The sample size, shape, and mechanical stress are compatible with integration in a vertical thermoelectric generator.

Further optimisation options (such as decreasing the overall porosity of the sample to reach higher electrical conductivity, and the use of more efficient dopants or the ion exchange doping method) are under investigation. The strategy can easily be applied to n-type materials to produce TE modules composed of low-cost and lightweight materials.

Conflicts of interest

There are no conflicts of interest to declare.

Data availability

The data supporting this article have been included as part of the supplementary information (SI). Supplementary information: discussion on the rational choice to study the P3HT : sPS 0.5 : 0.5 blend ratio, cryo-SEM images of the gel's structure in their native solvent, discussion on the stability of the dopant in the solvent, strain–stress curve under compression, nitrogen physisorption curve, DSC curves, SEM-EDX images, discussion on the S–σ relationship, discussion of the effect of doping on the thermal conductivity, structural analysis of the $FeCl_3$- and F_4TCNQ:$FeCl_3$-doped aerogel and WAXS pattern of F_4TCNQ powder, electrical conductivity values of the most representative samples after 100 days of storage in the glove box, and comparison of the TE of the aerogels with the literature. See DOI: **https://doi.org/10.1039/d5tc03145a**.

Any further relevant data are available from the authors upon reasonable request.

Acknowledgements

S. E. acknowledges the doctoral school ED 182 of the University of Strasbourg for financial support. This work of the Interdisciplinary Thematic Institute HiFunMat, as part of the ITI 2021–2028 program of the University of Strasbourg, CNRS and Inserm, was also supported by IdEx Unistra (ANR-10-IDEX-0002) and SFRI (STRAT'US project, ANR-20-SFRI-0012) under the framework of the French Investments for the Future Program. The CarMac platform of the ICS is acknowledged for DSC characterization studies. The PLAMICS microscopy facility, MINAMEC, and *Différi*X facilities of the ICS are recognized for their technical support and the use of their equipment. The contribution of the Carnot MICA Institute to the purchase of the PILATUS detector is gratefully acknowledged. The MEB-Cro platform (T. Ferté and C. Leuvrey) is acknowledged for the SEM-ED measurements. M. Brinkmann and the C3-Fab platform (ICube) are acknowledged for providing access to the Seebeck measurement setup and the collinear four-probe setup, both located in a glove box. C. Lambour, L. Hermann, and J.-P. Lamps are thanked for technical support.

References

1 S. Wang, J. Y. Oh, J. Xu, H. Tran and Z. Bao, *Acc. Chem. Res.*, 2018, **51**, 1033.
2 D. Beretta, N. Neophytou, J. M. Hodges, M. G. Kanatzidis, D. Narducci, M. Martin- Gonzalez, M. Beekman, B. Balke, G. Cerretti, W. Tremel, A. Zevalkink, A. I. Hofmann, C. Müller, B. Dörling, M. Campoy-Quiles and M. Caironi, *Mater. Sci. Eng., R*, 2019, **138**, 100501.
3 J. H. Bahk, H. Fang, K. Yazawa and A. Shakouri, *J. Mater. Chem. C*, 2015, **3**, 10362.
4 Z. Fan and J. Ouyang, *Adv. Electron. Mater.*, 2019, **5**, 1800769.
5 D. Scheunemann, E. Järsvall, J. Liu, D. Beretta, S. Fabiano, M. Caironi, M. Kemerink and C. Müller, *Chem. Phys. Rev.*, 2022, **3**, 021309.
6 J. Ding, Z. Liu, W. Zhao, W. Jin, L. Xiang, Z. Wang, Y. Zeng, Y. Zou, F. Zhang, Y. Yi, Y. Diao, C. R. McNeill, C.-A. Di, D. Zhang and D. Zhu, *Angew. Chem., Int. Ed.*, 2019, **58**, 18994–18999.
7 P. Durand, H. Zeng, B. Jismy, O. Boyron, B. Heinrich, L. Herrmann, O. Bardagot, I. Moutsios, A. Mariasevskaia, A. Melnikov, D. Ivanov, M. Brinkmann and N. Leclerc, *Mater. Horiz.*, 2024, **11**, 4737–4746.
8 S. A. Gregory, A. K. Menon, S. Ye, D. S. Seferos, J. R. Reynolds and S. K. Yee, *Adv. Energy Mater.*, 2018, **8**, 1802419.
9 D. Kiefer, R. Kroon, A. I. Hofmann, H. Sun, X. Liu, A. Giovannitti, D. Stegerer, A. Cano, J. Hynynen, L. Yu, Y. Zhang, D. Nai, T. F. Harrelson, M. Sommer, A. J. Moulé, M. Kemerink, S. R. Marder, I. McCulloch, M. Fahlman, S. Fabiano and C. Müller, *Nat. Mater.*, 2019, **18**, 149–155.

10 I. E. Jacobs, Y. Lin, Y. Huang, X. Ren, D. Simatos, C. Chen, D. Tjhe, M. Statz, L. Lai, P. A. Finn, W. G. Neal, G. D'Avino, V. Lemaur, S. Fratini, D. Beljonne, J. Strzalka, C. B. Nielsen, S. Barlow, S. R. Marder, I. McCulloch and H. Sirringhaus, *Adv. Mater.*, 2022, **34**, 2102988.

11 V. Vijayakumar, Y. Zhong, V. Untilova, M. Bahri, L. Herrmann, L. Biniek, N. Leclerc and M. Brinkmann, *Adv. Energy Mater.*, 2019, **9**, 1900266.

12 A. C. Hinckley, S. C. Andrews, M. T. Dunham, A. Sood, M. T. Barako, S. Schneider, M. F. Toney, K. E. Goodson and Z. Bao, *Adv. Electron. Mater.*, 2021, **7**, 2001190.

13 Y. Zhao, Z. Li, D. Wang, X. Zhang, Z. Ji, L. Niu, Y. Di, Y. Guan, L. Liu, Y. Zou, C. Li, F. Zhang, D. Zhang, D. Zhu and C. Di, *Adv. Mater.*, 2024, **36**, 2407692.

14 Q. Weinbach, C. B. Nielsen and L. Biniek, *J. Mater. Chem. C*, 2021, **9**, 10173–10192.

15 L. Liang, X. Wang, Z. Liu, G. Sun and G. Chen, *Chin. Phys. B*, 2022, **31**, 027903.

16 N. R. Radouane, *J. Sol-Gel Sci. Technol.*, 2023, **106**, 639–653.

17 M. P. Gordon, E. W. Zaia, P. Zhou, B. Russ, N. E. Coates, A. Sahu and J. J. Urban, *J. Appl. Polym. Sci.*, 2016, **134**, 44070.

18 Q. Weinbach, N. Hmili, E. Gottis, G. Fleith, J. Combet, V. Papaefthimiou, V. Malesys, E. Denys, L. Simon, M. Schmutz, A. Carvalho, D. Constantin and L. Biniek, *J. Mater. Chem. C*, 2023, **11**, 7802–7816.

19 J. Feng, Z. Zhuang, Y. Zhou and C. Li, *Adv. Funct. Mater.*, 2024, **34**, 2315188.

20 H. E. Baysal, T. Yu, V. Naenen, S. De Smedt, D. Hiz, B. Zhang, H. Xia, I. Florenciano, M. Rosenthal, R. Cardinaels and F. Molina-Lopez, *Adv. Sci.*, 2025, **12**, 2412491.

21 R. Kroon, J. D. Ryan, D. Kiefer, L. Yu, J. Hynynen, E. Olsson and C. Müller, *Adv. Funct. Mater.*, 2017, **27**, 1704183.

22 Q. Weinbach, S. V. Thakkar, A. Carvalho, G. Chaplais, J. Combet, D. Constantin, N. Stein, D. Collin and L. Biniek, *Front. Electron. Mater.*, 2022, **2**, 875856.

23 S. V. Thakkar, T. Nabiyeva, Q. Weinbach, H. Bhatia, Z. Liu, T. Ferté, C. Leuvrey, A. Carvalho, B. C. Schroeder and L. Biniek, *Polymer*, 2024, **296**, 126761.

24 N. Yanagishima, S. Kanehashi, H. Saito, K. Ogino and T. Shimomura, *Polymer*, 2020, **206**, 122912.

25 G. Zuo, H. Abdalla and M. Kemerink, *Adv. Electron. Mater.*, 2019, **5**, 1800821.

26 Y. Chang, Y. H. Huang, P. S. Lin, S. H. Hong, S. H. Tung and C. L. Liu, *ACS Appl. Mater. Interfaces*, 2024, **16**, 3764.

27 A. D. Scaccabarozzi and N. Stingelin, *J. Mater. Chem. A*, 2014, **2**, 10818.

28 N. Okada, K. Sato, M. Yokoo, E. Kodama, S. Kanehashi and T. Shimomura, *ACS Appl. Polym. Mater.*, 2021, **3**, 455.

29 G. Mano, Y. Murasawa, K. Shimamura, A. Iso, S. Kanehashi and T. Shimomura, *J. Appl. Polym. Sci.*, 2022, **139**, e52354.

30 C. Zhang, X. Liu, S. Han, M. Wu, R. Xiao, S. Chen and G. Chen, *Adv. Electron. Mater.*, 2025, 2400824.

31 K. Liu, J. Wang, X. Pan, S.-Y. Tian, Y. Liu, Z. Zhang, Y. Di, J. Chen, C. Wu, X.-Y. Deng, D. Wang, P. Li, C.-K. Pan, F. Qi, J. Liu, J. Hua, J. Pei, C.-A. Di, Y. Guo, Y. Liu and T. Lei, *Nature*, 2025, **644**, 920–926.

32 K. Samanta, J. M. Guenet and S. Malik, *Macromolecules*, 2019, **52**, 8569.

33 J. F. Rudd, in *Polymer Handbook*, ed. J. Brandrup and E. H. Immergut, John Wiley & Sons, Toronto, Canada, 3rd edn, 1989, pp. V/82.

34 T. J. Prosa, M. J. Winokur, J. Moulton, P. Smith and A. J. Heeger, *Macromolecules*, 1992, **25**, 4364–4372.

35 K. S. Walton and R. Q. Snurr, *J. Am. Chem. Soc.*, 2007, **129**, 8552–8556.

36 J. Rouquerol, P. Llewellyn and F. Rouquerol, *Stud. Surf. Sci. Catal.*, 2007, **160**, 49–56.

37 J. Balko, R. H. Lohwasser, M. Sommer and M. Thelakkat, *Macromolecules*, 2013, **46**, 9642–9651.

38 A. J. Pasztor, B. G. Landes and P. J. Karjala, *Thermochim. Acta*, 1991, **177**, 187–195.

39 S. Yilmaz, *J. Semicond.*, 2015, **36**, 082001.

40 A. Hamidi-Sakr, L. Biniek, J.-L. Bantignies, D. Maurin, L. Herrmann, N. Leclerc, P. Lévêque, V. Vijayakumar, N. Zimmermann and M. Brinkmann, *Adv. Funct. Mater.*, 2017, **27**, 1700173.

41 A. Danine, J. Schoenleber, J. Ghanbaja, F. Montaigne, C. Boulanger and N. Stein, *Electrochim. Acta*, 2018, **279**, 258–268.

42 C. Frantz, N. Stein, L. Gravier, S. Granville and C. Boulanger, *J. Electron. Mater.*, 2010, **39**, 2043–2048.

43 K. Tsutsui, T. Katsumata, H. Fukatsu, H. Yoshimizu, T. Kinoshita and Y. Tsujita, *Polym. J.*, 1999, **31**, 268–273.

44 G. M. Newbloom, K. M. Weigandt and D. C. Pozzo, *Macromolecules*, 2012, **45**, 3452–3462.

45 S. Berson, R. De Bettignies, S. Bailly and S. Guillerez, *Adv. Funct. Mater.*, 2007, **17**, 1377–1384.

46 V. G. Krishnan, A. M. Joseph, S. K. Peethambharan and E. B. Gowd, *Macromolecules*, 2021, **54**, 10605–10615.

47 L. Yu, D. Scheunemann, A. Lund, D. Kiefer and C. Müller, *Appl. Phys. Lett.*, 2021, **119**, 181902.

48 N. Kayunkid, S. Uttiya and M. Brinkmann, *Macromolecules*, 2010, **43**, 4961.

49 D. Dudenko, A. Kiersnowski, J. Shu, W. Pisula, D. Sebastiani, H. W. Spiess and M. R. Hansen, *Angew. Chem., Int. Ed.*, 2012, **51**, 11068–11072.

50 B. Gowd, K. Tashiro and C. Ramesh, *Prog. Polym. Sci.*, 2009, **34**, 280–315.

51 B. Gowd, N. Shibayama and K. Tashiro, *Macromolecules*, 2008, **41**, 2541–2547.

52 G. Guerra, V. M. Vitagliano, C. De Rosa, V. Petraccone and P. Corradini, *Macromolecules*, 1990, **23**, 1539–1544.

53 C. Daniel and G. Guerra, *Adv. Mater.*, 2005, **17**, 1515–1518.

54 L. Sanguigno, V. Venditto, G. Guerra and G. Mensitieri, *Polymer*, 2004, **45**, 429–436.

55 V. Untilova, T. Biskup, L. Biniek, V. Vijayakumar and M. Brinkmann, *Macromolecules*, 2020, **53**, 2441–2453.

56 M. F. Ashby, A. G. Evans, N. Fleck, L. J. Gibson, J. Hutchinson and H. N. G. Wadley, *Metal Foams: a Design Guide*, Butterworth-Heineman, Boston, 2000.

57 I. E. Jacobs, E. W. Aasen, J. L. Oliveira, T. N. Fonseca, J. D. Roehling, J. Li, G. Zhang, M. P. Augustine, M. Mascal and A. J. Moulé, *J. Mater. Chem. C*, 2016, **4**, 3454–3466.
58 A. M. Glaudell, J. E. Cochran, S. N. Patel and M. L. Chabinyc, *Adv. Energy Mater.*, 2015, **5**, 1401072.
59 Z. Liang, Y. Zhang, M. Souri, X. Luo, A. M. Boehm, R. Li, Y. Zhang, T. Wang, D.-Y. Kim, J. Mei, S. R. Marder and K. R. Graham, *J. Mater. Chem. A*, 2018, **6**, 16495.
60 X. Hao, J. Wang and H. Wang, *Chem. Soc. Rev.*, 2025, **54**, 1957–1985.